ISSN 0915-6364

NATIONAL INSTITUTE FOR FUSION SCIENCE

Opacity Free and Space Resolved X-ray Diagnostics Based on Satellinte Lines near H-like Lyα of Highly Charged Ions

N. Yamamoto, T. Kato and F.B. Rosmej

(Received - Mar. 19, 2004)

NIFS-DATA-88 Sep. 2004

TOKI, JAPAN

Opacity free and space resolved x-ray diagnostics based on satellite lines near H-like Lyα of highly charged ions

Norimasa Yamamoto[1], Takako Kato[2], and Frank B. Rosmej[3]

[1]Rikkyo University, Toshima, 171-8501, Japan

[2]National Institute for Fusion Science, Toki, 509-5292, Japan

[3]Université de Provence et CNRS, Centre de Saint Jérôme, PIIM, UMR 6633, 13397 Marseille cedex 20, France

Abstract

Space resolved high resolution spectroscopic methods have shown that dielectronic satellite emission in high energy laser produced plasmas is confined to the area of highest density and temperature. Employing satellite transitions near Lyα we demonstrate, that opacity free temperature and density diagnostic can be based solely on the satellite transitions $2lnl' \rightarrow 1snl' + h\nu$. The exclusion of the resonance line transition in the analysis provides an opacity free diagnostic method with limited need for spatial deconvolution.

For the interpretation of the experimental data we have developed a collisional-radiative model involving autoionising states with high n spectator electrons. The atomic data for dielectronic satellite transitions are calculated with different methods and compared also in view for diagnostic applications. For $n = 2$ satellite transitions we find in general good agreement, however, for higher quantum numbers n, the agreement of data is found to be not satisfactory.

Keywords: laser-produced plasma, H-like Mg ions, dielectronic satellites, collisional-radiative model, plasma diagnostics

1. Introduction

In high temperature and high density plasmas, satellite lines emitted through doubly excited states are important for plasma diagnostics. The dielectronic rcombination is related to ion abundances and satellite line emissions in plasma. Satellite lines have been widely used for plasma diagnostics of solar flares [1, 2], Tokamak plasmas [3, 4] and laser produced plasmas [5, 6], especially for dielectronic satellite lines of Li-like ions. For temperature diagnostics the intensity ratios of the satellite lines to the resonance line have been used because these ratios have a strong temperature dependence. The intensity ratios of the intercombination line $1s^2\ ^1S_0 - 1s2p\ ^3P_{1,2}$ or forbidden line $1s^2\ ^1S_0 - 1s2s\ ^3S_1$to the resonance line $1s^2\ ^1S_0 - 1s2p\ ^1P_1$, have been used for density diagnostics for He-like ions [7, 8]. However in high density plasmas such as laser produced plasmas, the resonance line is easily affected by opacity. Electron density of microplasma by vacuum-spark discharge has been measured using the density effect by inner shell excitation on the intensity of satellite lines [9] or by collisional transition 2s – 2p on the intensity ratio of $Ly\alpha_1$ to $Ly\alpha_2$ lines for high-Z ions [10] to be $10^{21}cm^{-3} \sim 10^{23}cm^{-3}$.
The large number of wavelength, transition probability, and intensity factor of satellite lines from H-, He-, and Li-like ions on various elements are calculated by Vinshtein and Safronova [11]. Satellite lines of various ions in laser-produced plasma are identified [12, 13] using these data.

In this paper we study the satellite lines of He-like ions in detail. We have made a collisional-radiative model (CRM) for H-like and He-like ions including the doubly excited states. X-ray spectra of H-like Mg ions were measured from a laser produced plasma with a high resolution spectrometer by F. B. Rosmej [14, 15]. We identify satellite lines for 1s*nl* lines ($n = 2 \sim 4$) and analyzed the spectra using our CRM. We compare three kinds of atomic data for spectral analysis. We derived temperatures of 180, 200, 210 eV at three points imaged by the spectrometer. The derived electron density is $5 \times 10^{20}\ cm^{-3}$.

We present in this paper a new method for diagnostics based on satellite lines only – this has great advantages: no opacity, limited need for spatial deconvolution and the similar set

of lines provides density, temperature and possibly even some indication of transient processes. The temperature sensitive intensity ratio of satellite lines is mainly used as the intensity ratios of $n = 3$ to $n = 2$ line ratios such as I_f (1s3d $^1F_3$ – 2p3d $^1F_3$) / I_J (1s2p $^1P_1$ – 2p^2 $^1D_2$). The density sensitive intensity ratio of satellite lines is the ratio of singlet and triplet lines such as I_A (1s2p $^3P_1$ – 2p^2 $^3P_1$) / I_J (1s2p $^1P_1$ – 2p^2 $^1D_2$). The intensity ratio I_T (1s2s $^1S_0$ – 2s2p $^1P_1$) / I_J (1s2p $^1P_1$ – 2p^2 $^1D_2$) is found to have no temperature and density dependence. This ratio is used to decide the background level. We have investigated the accuracy of atomic data by fitting the experimental data comparing the atomic data obtained by different methods especially for these intensity ratios.

We found that the higher order satellites are very important to obtain temperature sensitivity. The data of intensity factor for higher order satellites are investigated by comparing the different atomic data and measurement. It is found, that the data agreement is not completely satisfactory.

2. Experimental setup and line identification

X-ray line spectra with high spectral resolution ($\lambda/\Delta\lambda \sim 5000$) were measured at the nhelix-laser facility at GSI-Darmstadt [14, 15]. The laser is a 100 J Nd-Glass Laser (λ = 1.046 μm), with a pulse width of 15 ns and energy of 17 J. A massive Mg target is irradiated at normal incidence. Focal spot diameter onto the target is 500 μm. X-rays generated at the target are observed with spherically bent mica crystals in the second order of refraction providing simultaneous high spatial and spectral resolution. The angle between the direction of the observation and the target surface (z'-direction) is 45° and the spatial resolution through the direction is 14 μm. In this paper, we analyze spectra from three different directions: "center", "+170 μm" and "–170 μm", as shown in Figure 1. "Center" corresponds to the crossing points of the laser beam and the surface of the target. "+170 μm" corresponds to a position separated by 170 μm from "center" in the z-direction. "–170 μm" corresponds to a position below the "center" point.

The spectra measured from the center are sown in Figs. 2(a) and (b). These spectra include Lyα (1s $^2S_{1/2}$ – 2p $^2P_{1/2}$: 8.4192Å and 1s $^2S_{1/2}$ – 2p $^2P_{3/2}$: 8.4246Å) lines and many

dielectronic satellite lines ($1snl - 2l'nl$). We identified the observed satellite lines using the atomic data (wavelength, radiative transition rates, autoionization rates) calculated by Vainshtein and Safronova [11, 16]. Among the numerous satellite lines the strongest is the line J ($1s2p\ ^1P_1 - 2p^2\ ^1D_2$) at λ = 8.5513Å and most of the resolved lines are from $2l2l'$ states. As shown in Figure 2(b), $2l3l'$ satellite lines are also identified for H-like Mg ions. Most of the lines from $2l4l'$ and $2l5l'$ states are blended in Lyα lines. The line $1s4d\ ^3D_3 - 2p4d\ ^3F_4$ at 8.4326A is the strongest as n = 4 lines. In Table 1 the wavelengths used for identification are listed. In this paper, we will use the following symbols [17] to identify the satellite lines as shown in Table 1 and Figure 2(b).

3. Atomic Data

In order to interpret the observed spectra, atomic data are very important. We compare here with the three different theoretical data calculated using i) MZ code by Vainshtein and Safronova (MZ) [11, 16], ii) a code based on relativistic many-body perturbation theory combined with complex rotation by Lindroth (MBL) [18] and iii) a code based on relativistic many-body perturbation theory by Safronova (MBS) [19].

We compare the atomic data for satellite lines $1s2l - 2l'2l$, $1s3l - 2l'3l$, $1s4l - 2l'4l$, and $1s5l - 2l'5l$. Three atomic data sets by MZ, MBS, and MBL are compared in Table 2 for the wavelengths, radiative transitions, autoionization rates, and intensity factors Q^d,

$$Q^d = \frac{g_i A^r A^a}{\sum A^r + \sum A^a} \tag{1}$$

where g_i is the statistical weight of the upper state i, A^r is the radiative transition rate from level i to j, A^a is the autoionization rate of level i. The data by MZ are designated assuming LS coupling and those by MBS and MBL assume jj coupling scheme. In Table 2 we list the configuration in LS coupling. The correspondences of jj coupling for MBS and MBL to LS coupling are given by authors. The atomic data for transitions with large Q^d which are mainly $\geq 10^{13}$ s^{-1} are listed in Table 2. Generally for $2l2l'$ and $2l3l'$ lines, agreements are

good. Large differences are found for $2l4l'$ and $2l5l'$ lines between MZ and many-body theory (MBS and MBL). In the following, the differences of atomic data are represented by percentages, which are one hundred times of MBS/MZ – 1 and MBL/MZ – 1, respectively.

In order to get insight in the diagnostic stability employing different set of atomic data MZ, MBS, and MBL, we present in figure 3 simplified spectral distributions; for (a) $n = 2$, (b) $n = 3$, (c) $n = 4$ and (d) $n = 5$ transitions are convoluted with an intensity factor, $Q^d \times P(\lambda)$, where $P(\lambda)$ is the Voigt line profile, more detailed of $P(\lambda)$ are discussed in eq.(7) in Sec. 5.

Most of the data for $1s2l - 2l'2l$ transitions, the A^a and A^r values agree within ± 20%. The difference in intensity factor Q^d for these transitions are about 10%. The largest difference for A^a value is 30% for the $2p^2\ ^3P_2$ state, which is the upper state of line A. The disagreement in Q^d for A line is also 30% for both MBS and MBL data. This difference results in a great error for the density diagnostics which will be discussed in Sec. 4; the difference could be enormous, e.g., instead of a density 2×10^{20} one could diagnose 7×10^{20} cm^{-3}. For J line ($1s2p\ ^1P_1 - 2p^2\ ^1D_2$), which has the largest A^a in satellite lines, wavelength of MBS is 1.6mÅ shorter than MZ and MBL. Concerning to the wavelength relations among J, T and Lyα, MBL is better than those by MZ and MBS.

The difference for $1s3l - 2l'3l$ transitions are larger than those for $1s2l - 2l'2l$ transitions. The differences of A^a for $2p3d\ ^1F_3$, the upper level of line f, are 40% for MBS and 5% for MBL, and the differences of Q^d are 13% for MBS and –7% for MBL, respectively. This line is diagnostically important because it strongly influence the temperature parameter. Comparing to the measurement, we have an impression MZ data is better than MBS and MBL as will be discussed later. In the wavelength range of 8.43 ~ 8.44Å, there are three main lines, $1s3p\ ^3P_2 - 2p3p\ ^1D_2$, $2s3d\ ^3D_2$, and $2p3p\ ^3P_2$, by MZ representation. These three lines have two Q^d with $1 - 2 \times 10^{13} s^{-1}$ and one Q^d with order of $10^{11} s^{-1}$. We find differences between MZ and MBS for Q^d values for these three lines. It is considered that this difference is due to the identification of the lines by different LS and jj scheme. As shown in Figure 3(b) the overall spectral distribution is not much different with three data sets. The spectrum in 8.44 ~ 8.46Å consists of several relatively strong lines. These lines also

have disagreement in identifications. However the convoluted spectra agrees well with each other. The strongest line in this wavelength range is $1s3d\ ^3D_3 - 2p3d\ ^3F_2$ and the atomic data for this transition agree well.

Data for $1s4l - 2l'4l$ transitions have much larger discrepancy than those for $n = 2$ and 3. Especially, A^a values by MZ for $2p4f\ ^3D_{1,2,3}$, which are the upper states of satellite lines in the wavelength range of 8.4157 – 8.4158Å, are larger by $1 \sim 4$ order of magnitude than those by MBS and MBL. Therefore, Q^d values of these transitions by MZ are also larger by $1 \sim 3$ order of magnitude than MBS and MBL.

For $n = 5$ transitions, Q^d values of transitions from the upper states $2s5f\ ^3F$ and $2p5f\ ^3D$ by MBL are smaller by factor $10 \sim 10^3$ than those by MZ, because the autoionization rate by MBL is smaller than MZ by factor $10^2 \sim 10^4$. Therefore the large difference is found at around 8.417Å as shown in Figure3 (d). The Q^d value for $1s5d\ ^3D_3 - 2p5d\ ^3F_4$ (8.4260Å) transition by MBL is 20% of that by MZ since the autoionization rate is about 20% and the radiative transition rate is 30% of those by MZ.

4. Collisional-radiative Model for satellite lines

Usual collisonal-radiative models (CRM) include only singly excited states and the doubly excited states, which lie under a singly excited state, are not explicitly included. However, we observe many satellite lines which are emitted through the doubly excited sates in X-ray spectra from laser produced plasmas, solar flares, magnetic confined plasmas such as tokamak. In order to obtain temperature and density sensitivity on the solely basis of satellite transitions it is necessary to calculate their population densities explicitly by means of a CRM. We have constructed a CRM of H-like and He-like system including the He-like doubly excited states, including the $n = 2$ (2s and 2p) levels for H-like ions [20] and the levels up to $n = 3$ (3s, 3p and 3d) for H-like levels [21]. In this paper we have developed this model including $2lnl'$ levels with fine structure resolved levels for $n = 2$, 3, 4 and 5.

4.1 Energy Level

In our CRM the ground state $1s^2$ and singly excited states $1snl$, doubly excited states $2l'nl$ and $3l'nl$ for He-like ions, and 1s, $2l$, and $3l$ states for H-like ions are included. The total number of levels is 367: $1snl$ (60 states), $2l'nl$ (230 states), and $3l'nl$ (70 states). For singly excited states $1snl$, $n = 2$ states are resolved in fine structure levels, for the states with $3 \le n \le 7$ are averaged with total angular moment J, for the levels with $8 \le n \le 10$ are averaged with angular moment L separating by spin, and for the levels with $11 \le n \le 20$ are averaged into the principal quantum number n [22]. For doubly excited states $2l'nl$, with $2 \le n \le 5$ are resolved into fine structure levels, and the levels with $6 \le n \le 20$ are combined into the averaged excited states as $1snl$ states in He-like CRM. For doubly excited states $3l'nl$, $n = 3$ levels are averaged with total angular moment J, and $4 \le n \le 20$ are averaged with orbital quantum number l. In Figure 4 the schematic energy level diagram for our CRM is shown.

For $2l'nl$ states with $2 \le n \le 5$ we used the detailed atomic data for radiative decay and autoionization rates calculated by MZ, MBS and MBL. For the levels with $6 \le n \le 20$, the data scaled following Ref. [22] are used. For $3l'nl$ states with $n = 3$, 4 and 5, the data calculated by Hullac code [23] are used. For the levels with $6 \le n \le 20$, the data for autoionization rate are scaled using n^{-3} formula and for the transition probabilities for $3l'nl - 1snl$ and $3l'nl - 2l''nl$ are used to be H-like ion values of $3l' - 1s$ and $3l' - 2l''$ transitions, respectively.

4.2 Rate equation

An Emission line intensity is calculated using a population density of an upper level multiplied by a radiative transition rate. Population densities are obtained by solving the following equations,

$$\frac{dN_i}{dt} = -\sum_j W_{ij} N_i + \sum_j W_{ji} N_j , \qquad (2)$$

where W_{ji} is a total transition rate from j state to i state.

Atomic processes considered in our model are excitation / de-excitation, ionization / three-body recombination, radiative recombination and dielecronic capture by electron impact, radiative transition and autoionization. Collisional atomic data (excitation and ionization) for singly excited states 1snl and for doubly excited states $2l'nl$ are the same as used in ref. [21]. Collisional excitation rate coefficients between doubly excited states $2l2l'$ are taken from Goett et al. [24] and from 1s$2l$ to $2l'2l''$ are taken from ref. [25]. The transition rates between doubly excited states $3l'nl$ are calculated using HULLAC code [23].

Eq.(2) are solved assuming quasi-steady state for doubly and singly excited states. Under this assumption we can write the steady state population densities N_i of excited states as a linear combination of the population densities of $1s^2$, 1s, 2s, 2p, 3s, 3p and 3d as follows,

$$N_i = \sum_y r_i^y N_e N_y , \tag{3}$$

where r_i^y and N_e are the population density coefficient and the electron density, respectively. Suffix y indicates the ground states of He-like ions $1s^2$ and H-like ions 1s, and excited states on H-like ions (2s, 2p, 3s, 3p and 3d).

Line intensities are then obtained by multipling the population density N_i, and radiative transition rate A^r as follows,

$$I_s = N_i A^r . \tag{4}$$

4.3 T_e- and N_e-dependence of satellite line intensity ratios

Since satellite line intensities depend on electron temperature T_e and density N_e, the satellite line intensity ratios depend on T_e and N_e. The intensities in this section are calculated in equilibrium condition in eq. (3).

Density dependence is mainly caused by the collisional process through l changing with

the same n. Electron density dependence for several line intensity ratios of satellite lines at T_e = 200eV are shown in Figure 5 by two different atomic data, MZ and MBL. Among intensity ratios, I_A ($1s2p\ ^3P_2 - 2p^2\ ^3P_2$) / I_J ($1s2p\ ^1P_1 - 2p^2\ ^1D_2$) has the strong dependence as shown in Figure 5. Since dielectronic capture rate to $2s2p\ ^3P_2$ is larger than that of $2p^2\ ^3P_2$ by factor 5, and total depopulating rates from these states are almost the same, the population densities of these states are N ($2s2p\ ^3P_2$) > N ($2p^2\ ^3P_2$) at low-densities. With increasing electron density, population density of $2p^2\ ^3P_2$ increases by l-changing collisional-excitation from $2s2p\ ^3P_2$ state. On the contrary the population density $2s2p\ ^3P$ is decreased by l-changing collisions. Therefore the ratio I_A ($1s2p\ ^3P_2 - 2p^2\ ^3P_2$) / I_J($1s2p\ ^1P_1 - 2p^2\ ^1D_2$) increases with increasing density for $N_e \geq 10^{19}$cm^{-3}. Ratio of I_Q ($1s2s\ ^3S_1 - 2s2p\ ^3P_2$) / I_J ($1s2p\ ^1P_1 - 2p^2\ ^1D_2$) gradually decrease over $N_e = 10^{20\text{-}21}$cm^{-3}. The ratio I_f ($1s3d\ ^1D_2 - 2p3d\ ^1F_3$) / I_J ($1s2p\ ^1P_1 - 2p^2\ ^1D_2$) also decreases at higher densities than 10^{21}cm^{-3}. The ratio I_T ($1s2s\ ^1S_0 - 2s2p\ ^1P_1$) / I_J ($1s2p\ ^1P_1 - 2p^2\ ^1D_2$) has no dependence on electron density. On the other hand, intensity ratio I_A / I_J can be used for electron density diagnostics in the electron density range $N_e \geq 10^{20}$cm^{-3}. Electron density derived from I_A / I_J by MBL gives larger values than that by MZ.

Electron temperature dependence of several line intensity ratios at $N_e = 10^{20}$cm^{-3} are shown in Figure 6. The ratio I_J / $I_{Ly\alpha}$ drastically decreases with increase of temperature. This intensity ratio has been often used to estimate electron temperature in high temperature plasmas. However in our case we do not use this ratio because Lyα might be affected by opacity as mentioned in Sec.2. The intensity ratios, which have the same n quantum number as an upper state, have no temperature dependence. The line intensity ratios with different quantum numbers n as upper states such as, I_f / I_J can be used to estimate temperature, although dependence on temperature of intensity ratio I_f / I_J is much weaker than I_J / $I_{Ly\alpha}$. The intensity ratio I_f / I_J is written as

$$\frac{I_f^0}{I_J^0} \sim \frac{Q_f^d}{Q_J^d} exp\left(\frac{E_J - E_f}{kT_e}\right), \tag{5}$$

where I^0 is a line intensity at low density limit and E is the energy of the doubly excited state measured from the threshold (1s state). On the contrary independence on temperature and density for the ratio I_T / I_J can be used to define a reference line ratio in the measured spectra. The atomic data for two transitions by different method agree very well as seen in Table 2. Therefore this line ratio can be used as reference of line ratios.

4.4 Effect of inner shell excitation from He-like ions

In the previous 4.3 section, we considered a dielectronic capture populates the doubly excited states; $1s + e^- \rightarrow 2pnl$ as a population mechanism. However there is a possibility to populate the doubly excited states by inner shell excitation from the singly excited states $1snl$, $1s^2 \rightarrow 1snl \rightarrow 2pnl$ by electrons or photons. Another possible process is cascade processes from other doubly excited states, $1s + e^- \rightarrow 2l'nl$ ($n \geq 3$) $\rightarrow \ldots \rightarrow 2l'2l$.

Ion abundances and population densities of H-like and He-like ions in ionization equilibrium are shown in Figure 7 as a function of electron temperature for $N_e = 10^{20}$ cm^{-3}. In the temperature region $T_e < 300$eV, the population density of $1s^2$ state is largest among other states. Therefore in this temperature range, the contribution of the inner shell excitation processes to the intensities of satellite lines $1s2l - 2l'2l$ has importance. Cascade effects are important for the levels whose population densities are small like a $2p^2\ ^3P$ state.

We have studied the contribution of dielectronic capture, cascade, and inner shell excitation on the population densities of doubly excited states. Figure 8(a), (b), and (c) show the fractions of three processes (dielectronic capture, cascade, and inner shell excitation) in populations of $2l2l'$ states as a function of electron density at $T_e = 200$eV. Doubly excited $2l2l'$ states except $2p^2\ ^3P$ states are produced mainly by dielectronic capture at $N_e < 10^{22}$cm^{-3}. For $N_e > 10^{22}$cm^{-3}, l-changing transitions become dominant and the population densities are decided only by collisions. Then the population densities are proportional to statistical weight. On the other hands, density dependence of contributions on the $2p^2\ ^3P$ states is complicated because of autoionization rates of $2p^2\ ^3P$ is smaller than that of other states by about one order of magnitude. Fractions of population density of $2p^2\ ^3P_2$ state, which corresponds to line A, is also populated by dielectronic capture at $N_e <$

10^{22}cm^{-3} and l-changing transitions at $N_e > 10^{22}$cm^{-3}. The contribution of inner shell excitation from He-like ions is about 10% for a satellite d line ($1s2p\ ^3P_2 - 2p^2\ ^3P_2$) and less than 1% for other satellite lines.

Influence of photo absorption excitation $1s2l \rightarrow 2l'2l$ depends on geometry of real plasmas. For a satellite line A, $2p^2\ ^3P_2 \rightarrow 1s2p\ ^3P_2$, a mean free path is a few centimeters where optical depth becomes unity under the condition of $N\ (1s2p^3P_2) = 1.4 \times 10^{16}$ cm^{-3} with $N_e = 5 \times 10^{20}$ cm^{-3}. The size of the plasma, which we measure, is considered less than 1 mm. Therefore effect of opacity for satellite lines is negligible in our experiment.

On the other hands, mean free path of Lyα is several hundred micrometer which is much smaller that of satellite lines. Therefore the intensity of Lyα is affected by opacity very much which can be seen clearly from the observed spectra in Figure 2(a).

5. Spectral analysis

We analysed three kind of spectra measured from "Center", "–170μm", and "+170μm" as discussed in Sec.2. The intensity ratio I_f / I_j has a strong temperature dependence and I_A / I_j has density dependence as shown in Section 4.3. We used mainly these two intensity ratios to derive the electron temperature and density. Among three kind of atomic data compared in Table 2 in Sec. 2., we used two kinds of atomic data of MZ and MBL for our spectral analysis and compared the derived plasma parameters. The satellite line intensities are calculated by our collisionsal radiative model including the dielectronic states. Ionization equilibrium is assumed in our analysis.

5.1. Line Profile

In order to analyze the observed spectra we have to take into account the line profiles $P(\lambda)$, for a line intensity,

$$I_s(\lambda) = N_i A^r P(\lambda) \tag{6}$$

Since the wavelength resolution of the spectrometer is very high, it is necessary to find a

precise spectral profile in order to fit the observed spectra well. We used a Voigt profile as follows,

$$P(\lambda)=\int_0^{\infty}\frac{(\gamma+w)/2\pi}{(\lambda-\lambda')^2+(\gamma+w)^2/4}\frac{1}{\sigma\sqrt{\pi}}exp\left[-\left(\frac{\lambda-\lambda'}{\sigma}\right)^2\right]d\lambda' \qquad (7)$$

where λ_0 is the wavelength of the observed line, σ is the Doppler width (FWHM = 2.35σ), γ is the natural width (= FWHM) and w is the instrumental width. The natural width is given by the autoionization rate and radiative transition rate. The collisional processes are not included in the line width. The instrumental width w and Doppler width σ are derived from the observed line profile of J and T in the "Center" spectrum in order to approach closest to the maximum resolution. Since the intensity ratio I_T / I_J is constant for any plasma condition, the background level is decided to fit well I_T/ I_J. The instrumental width w = 0.5mÅ and the effective ion temperature 200eV for the Doppler width $\sigma$are obtained. Figure 9 shows an observed line profile of J together with calculated ones with the values of w = 0.5mÅ assuming $T_i = T_e$ = 200eV. The autoionzation rate of the upper state of line J is $A^a(2p^2\ ^1D_2) = 3.7 \times 10^{14}s^{-1}$ which is the strongest in satellite lines of He-like Mg ions. The natural width for J is γ= 1.44mÅ which can be compared with the observed FWHM = 3.3mÅ.

5.2 Center

Theoretical spectra using the atomic data by MZ and MBL are shown by dotted lines in Figures 10(a) and (b), respectively. In MZ case, the electron density N_e is obtained approximately to be $5 \times 10^{20}cm^{-3}$. If $N_e < 5 \times 10^{20}cm^{-3}$, the intensity of line A is too weak, while the intensities of lines Q, R and S are too weak for $N_e > 5 \times 10^{20}cm^{-3}$. The temperature T_e = 200eV is derived from the intensity ratio I_f/ I_J with MZ atomic data. This temperature corresponds to the high temperature limit to fit the wavelength range near the foot range of Lyα. When we use the atomic data by MBL, the derived temperature T_e = 230eV which is higher than that by MZ because of the difference of atomic data for the f

line. Two broad peaks near 8.43 ~ 8.44Å and 8.44 ~ 8.46Å, consist with many number of satellite lines not only from $2l3l'$ but also $2l4l'$ and $2l5l'$. They are in good agreement with the measured spectra in the case of MZ. In shorter wavelength side of Lyman α the calculated spectrum exceeds the measured spectrum as seen in Figure 10. This excess comes from mainly 1s4f – 2p4f lines which are much stronger by MZ than MBL as discussed in section 3.1. Theoretical spectral feature near Lyα foot with MBL atomic data agrees with the measured spectra better than that by MZ. Although the satellite lines in 8.44 ~ 8.46Å are in good agreement, the theoretical spectra in 8.43 ~ 8.44Å is too small in the case of MBL. The line intensity ratio I_T / I_J does not depend on temperature and density and should be constant for any conditions as shown in Figure 5 and 6. This intensity ratio can be used to determine the background level. We derived the background level considering the intensity ratio of I_T / I_J. However as seen in Figure 10, the theoretical intensity of line T is always smaller than the observed intensity. Since it was used a single Mg target with a purity of more than 99.9%, it is difficult to consider a blended line. The ion temperature for Gaussian component is assumed to be T_i = 200 eV for theoretical spectra. This value is derived from the line width of J and T as described in Sec.5.1.

From spectral fits shown in Figure 10, atomic data by MZ fit better than MBL for the satellite lines with $n \leq 4$. However for the satellite lines with $n = 5$, MZ data are too large comparing to the experiment and MBL data fit better. Figure 11 shows theoretical satellite line spectra separated for $1s2l - 2l'2l$, $1s3l - 2l'3l$, $1s4l - 2l'4l$ and $1s5l - 2l'5l$ components with MZ atomic data at T_e = 200eV and $N_e = 5 \times 10^{20}$cm^{-3} corresponding to best fit spectra.

5.3 –170μm

Comparison with the measured and theoretical spectra using atomic data for "–170μm" by MZ are shown in Figure 12. As is shown in Figure 12, the observed intensity of line f is weaker for the spectrum from "–170 μm" than that from "center". Therefore it is expected the lower electron temperature than that from "center". The electron temperature T_e = 180eV and electron density $N_e = 4 \times 10^{20}$cm^{-3} are derived from the intensity ratios of I_f / I_J and I_A / I_J respectively with atomic data by MZ. Using the data by MBL T_e = 200eV and N_e

$= 5 \times 10^{20}$cm^{-3} are derived. Satellite line spectra in 8.43 ~ 8.44Å are in good agreements for the spectrum by MZ. Higher temperature does not give a good agreement for a line f and satellite lines in 8.43 ~ 8.44Å in the case of MZ.

The calculated intensity for line T is larger than the measured one. T_e = 220eV and N_e = 3×10^{20}cm^{-3} are good parameters to fit the measured spectra in 8.44 ~ 8.46Å with MBL atomic data. However these temperatures are too high to explain the intensity of line *f* as shown in Fig.12. It is difficult to find a temperature to fit both line *f* and near Lyα lines.

In Figure 12, the calculated spectra with T_e = 150, 180, 220eV and $N_e = 4 \times 10^{20}$cm^{-3} are shown with measurement.

5.4 +170mkm

The spectrum measured from "+170μm" is shown in Figure 13. The intensity of f line is stronger than the case of "center" and "–170μm". The electron temperature T_e = 300eV is obtained from the intensity ratio I_f / I_J. However the intensities near Lyα are too strong with T_e = 300eV. Considering whole spectrum in all the wavelength range, we derive T_e = 210eV, $N_e = 5 \times 10^{20}$ cm^{-3} as a best fit with atomic data by MZ and T_e = 230eV and $N_e = 5 \times 10^{20}$ cm^{-3} with atomic data by MBL. Figure 13 show the comparison with the calculated spectra and measurement with three different densities.

Generally the intensities between 8.43 ~ 8.44A (mainly n = 4 lines) by MBL are too small for the measurements, although the results by MZ agree rather well with measurements.

6. Summary and Discussions

We have constructed CRM including doubly excited states and analyzed X-ray spectra of H-like Mg ions measured at GSI. We identified satellite lines for *2l2l'*, *2l3l'* and *2l4l'* transitions from the measured spectra.

We study the density and temperature dependences of satellite line intensity ratios. We proposed the new method for plasma diagnostics using only satellite line intensity ratios for temperature and density diagnostics. We compared three kinds of atomic data; MZ,

MBL and MBS for spectral analysis carefully. We found a better spectral fit with MZ data than MBL and MBS in 8.43 ~ 8.44Å (2*l*4*l*' lines). However MBL is better than MZ near 8.415 Å (2*l*5*l*' lines).

The plasma parameters are derived with the satellite line intensity ratios. The derived parameters are T_e = 200 ± 10 eV and N_e = 5 ± 2 ×10^{20} cm^{-3} for the "center" position, T_e = 210 eV and N_e = 5 × 10^{20} cm^{-3} for "+170μm" and T_e = 180 eV and N_e = 4 × 10^{20} cm^{-3} for "−170μm". The different temperatures from different directions are derived.

Acknowledgements:

Authors acknowledge offering of atomic data with Dr. U. I. Safronova and Dr. E. Lindroth. This work is partly supported by the collaboration programs of NIFS.

References

[1] Bely-Dubau, J. Dubau, P. Faucher, A.H. Gabriel, M. Loulergue, L. Steenman-Clark, S. Volonte, E. Antonucci, C.G. Rapley, Mom. Not. R. Astron. Soc. **201** 1155 (1982).

[2] J. Dubau and S. Volontr, Rep. Prog. Phys. **43** 199 (1980).

[3] M. Bitter et al , Phys. Rev. A **29** 661 (1984).

[4] T. Kato, S. Morita, K. Masai and S. Hayakawa, Phys. Rev. A **36** 795 (1987).

[5] A. Demir, P. Zeitoun, G.J. Tallents, et al., Phys. Rev. E **55** 1827 (1997).

[6] T. Fujimoto, N. Yamaguchi, J. Mizui, T. Kato and F. Fujita, J. Phys. D **14** 439 (1981).

[7] Vinogradov, A.V., Skobelev, I.Yu., Yukov, E.A., Sov. J. Quant. Electron. **5** 630 (1975).

[8] T. Fujimoto and T. Kato, Phys. Rev. A **30** 379 (1984).

[9] J. F. Seely and T. N. Lee, Phys. Rev. A **29** 411 (1984).

[10] A. Schulz, R. Burhenn, F. B. Rosmej and H. J. Kunze, J. Phys. D **22** 659 (1989).

[11] L. A. Vainshtein and U. I. Safronova, ADNDT **25** 311 (1978).

[12] J. F. Seely, Phys. Rev. Lett **42** 1606 (1979).

[13] J. F. Seely, R. H. Dixon and R. C. Elton, Phys. Rev. A **23** 1473 (1981).

[14] F. B. Rosmej et al., JETP Lett. **70** 270 (1999).

[15] F. B. Rosmej et al., Phys. Rev. A**63** 032716 (2001).

[16] U. I. Safronova, private communications.

[17] S. A. Pikuz, D. A. Hammer, D. H. Kalantar, A. Ya. Faenov, and I. Yu. Skobelev, Phys. Rev. A**49** 3450 (1994).

[18] M. Tokman, N. Eklöw, P. Glans, E. Lindroth, R. Schuch, G. Gwinner, D. Schwalm, A. Wolf, A. Hoffknecht, A. Müller, and S. Schippers, Phys. Rev. A **66** 012703 (2002).

[19] U. I. Safronova, private communications.

[20] T. Kato, N. Yamamoto, R. More, and T. Fujimoto, JQSRT **71** 431 (2001).

[21] N. Yamamoto, T. Kato, and T. Fujimoto, J. Plasma Fusion Res. **78** 1 (2002).

[22] T. Fujimoto and T. Kato, Phys. Rev. A. **32** 1663 (1985).

[23] A. Bar-Shalom, M. Klapisch and J. Oreg, Phys. Rev. A **38** 1773 (1988).

[24] S. T. Goett, D. H. Sampson and R.E.H. Clark, ADNDT **28** 279 (1983).

[25] D. H. Sampson, S. J. Goett and R. E. H. Clark, ADNDT **28** 299 (1983

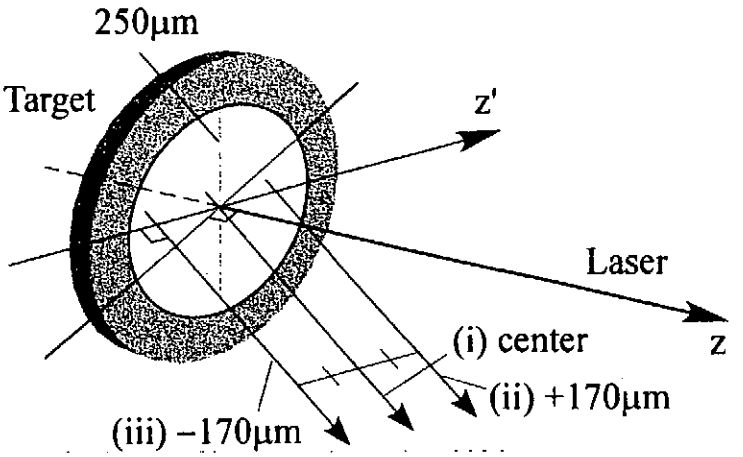

Figure 1. Experimental geometry for the measurement of satellite lines from a laser-produced Mg ion plasma. The measured spectra are obtained at three distances: "Center" corresponds to the crossing position with the laser and the surface of the target, "+170μm" corresponds to the position separated by 170μm from "center" to normal direction, "-170μm" corresponds to the position separated from "center" to surface direction.

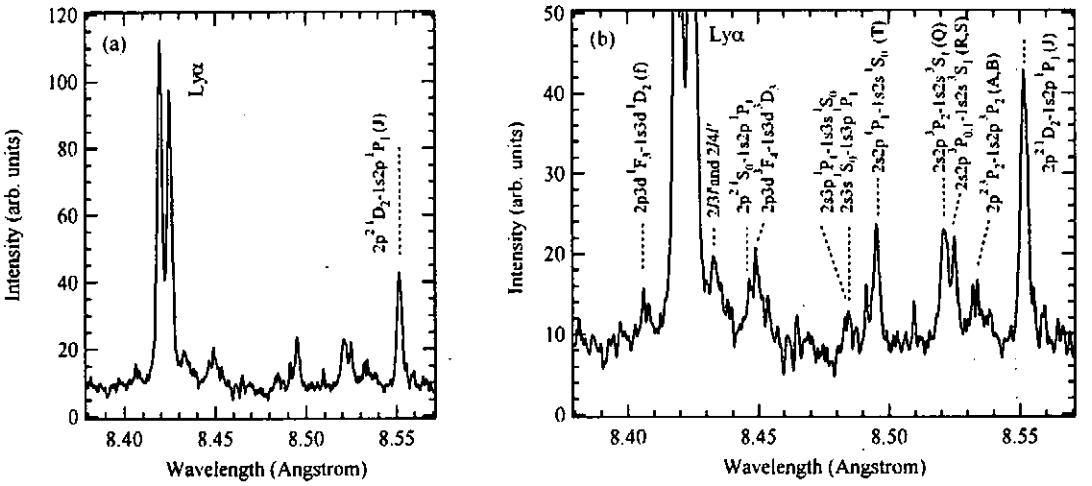

Figure 2. (a) The measured spectrum near H-like Mg Lyα lines. The spectrum is obtained from "center". (b) The measured spectrum near Lyα lines with identification for satellite lines.

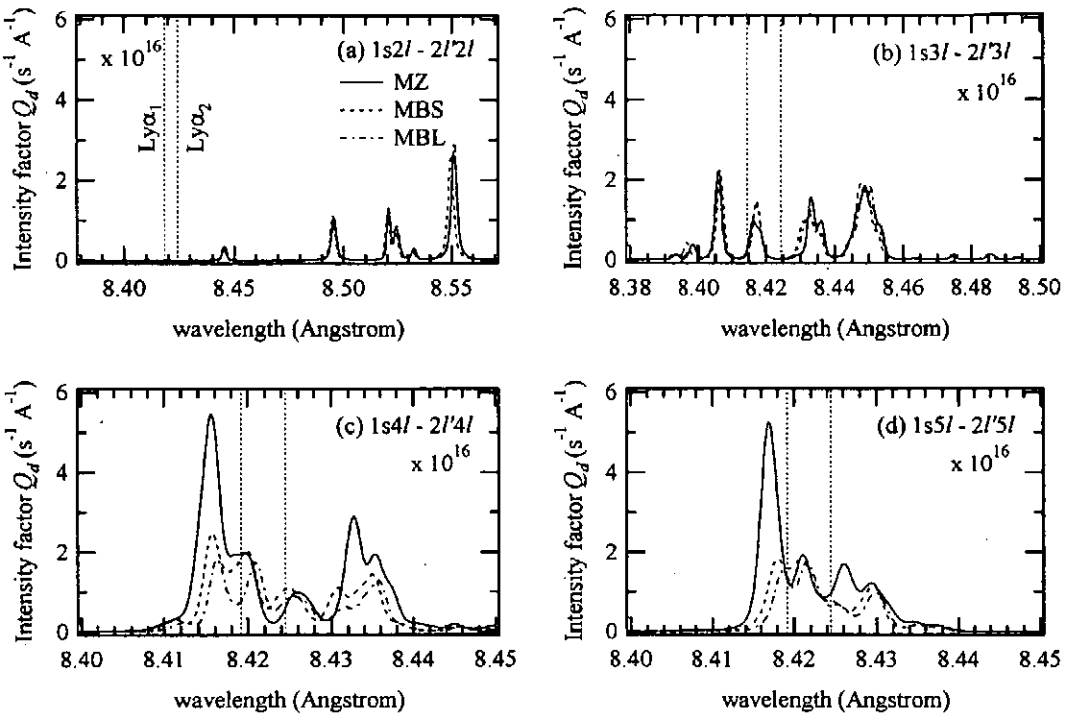

Figure 3. Comparison of intensity factor convoluted by the Voigt profile function for three different atomic data by MZ (solid line), MBS (dotted line), and MBL (dot-dashed line), respectively. Ion temperature T_i = 200eV and instrumental width 0.5mÅ are assumed. (a) 1s2l – 2l'2l, (b) 1s3l – 2l'3l, (c) 1s4l – 2l'4l and (d) 1s5l – 2l'5l transitions.

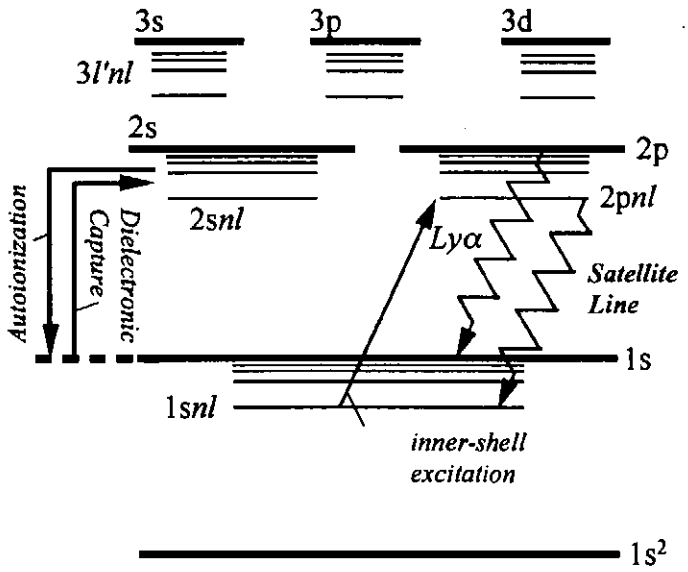

Figure 4. The schematic energy level diagram for our CRM.

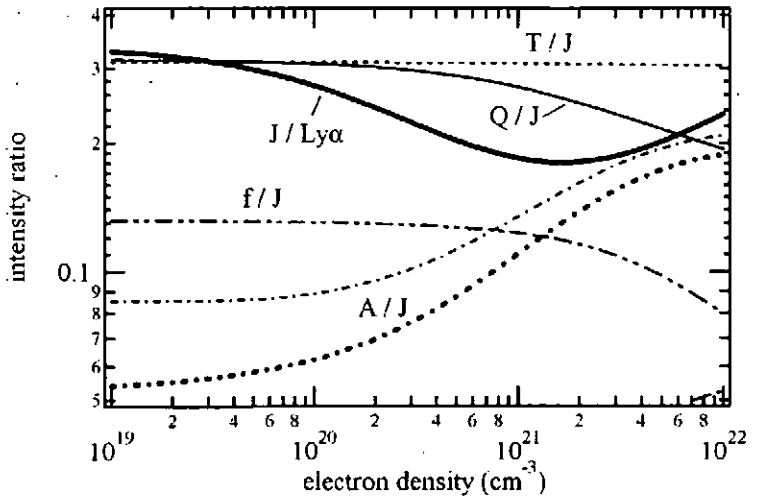

Figure 5. Density dependence of theoretical line intensity ratio at T_e = 200eV in an ionization equilibrium. Thin lines are intensity ratios by MZ for I_Q / I_J (solid line), I_T / I_J (dotted line), I_A / I_J (dot-dashed line) and I_f / I_J (dot-dot-dashed lines). Bold dot dashed line is for I_A / I_J by MBL.

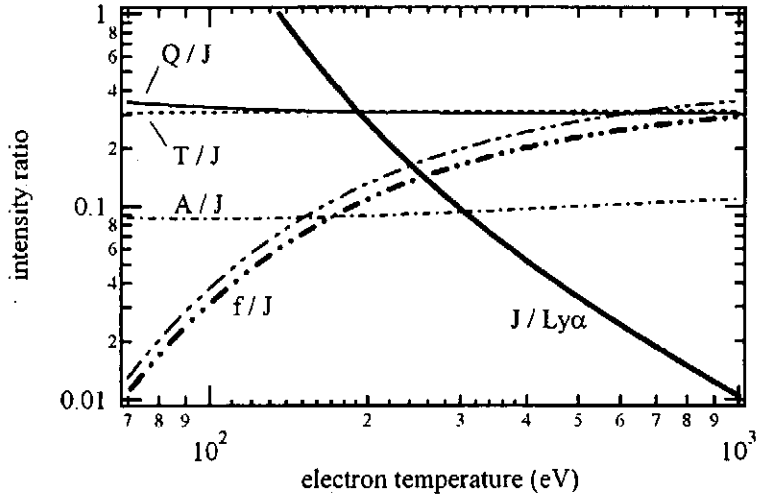

Figure 6. Temperature dependence of theoretical line intensity ratio at $N_e = 10^{20}cm^{-3}$ in an ionization equilibrium. Bold solid line is for I_J / $I_{Ly\alpha}$. Thin lines are intensity ratios by MZ for I_Q / I_J (solid line), I_T / I_J (dotted line), I_A / I_J (dot-dashed line) and I_f / I_J (dot-dot-dashed lines). Bold dot dot dashed line is for I_f / I_J by MBL.

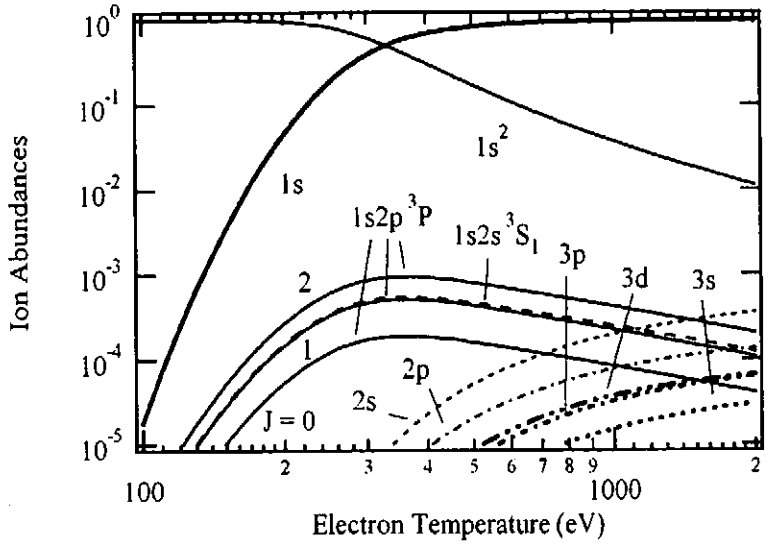

Figure 7. Ion abundances of Mg ions at $N_e = 10^{20}cm^{-3}$ in ionization equilibrium plasma. Thin solid line indicates $1s^2$ state, bold solid line 1s state. The excited states 1s2p ^{3}P (solid lines) and 1s2s ^{3}S (dashed line) for He-like ions and 2s (dashed), 2p (dot-dashed), 3s (dotted), 3p (dot dashed) and 3d (dot-dot dashed) for H-like ions are also shown.

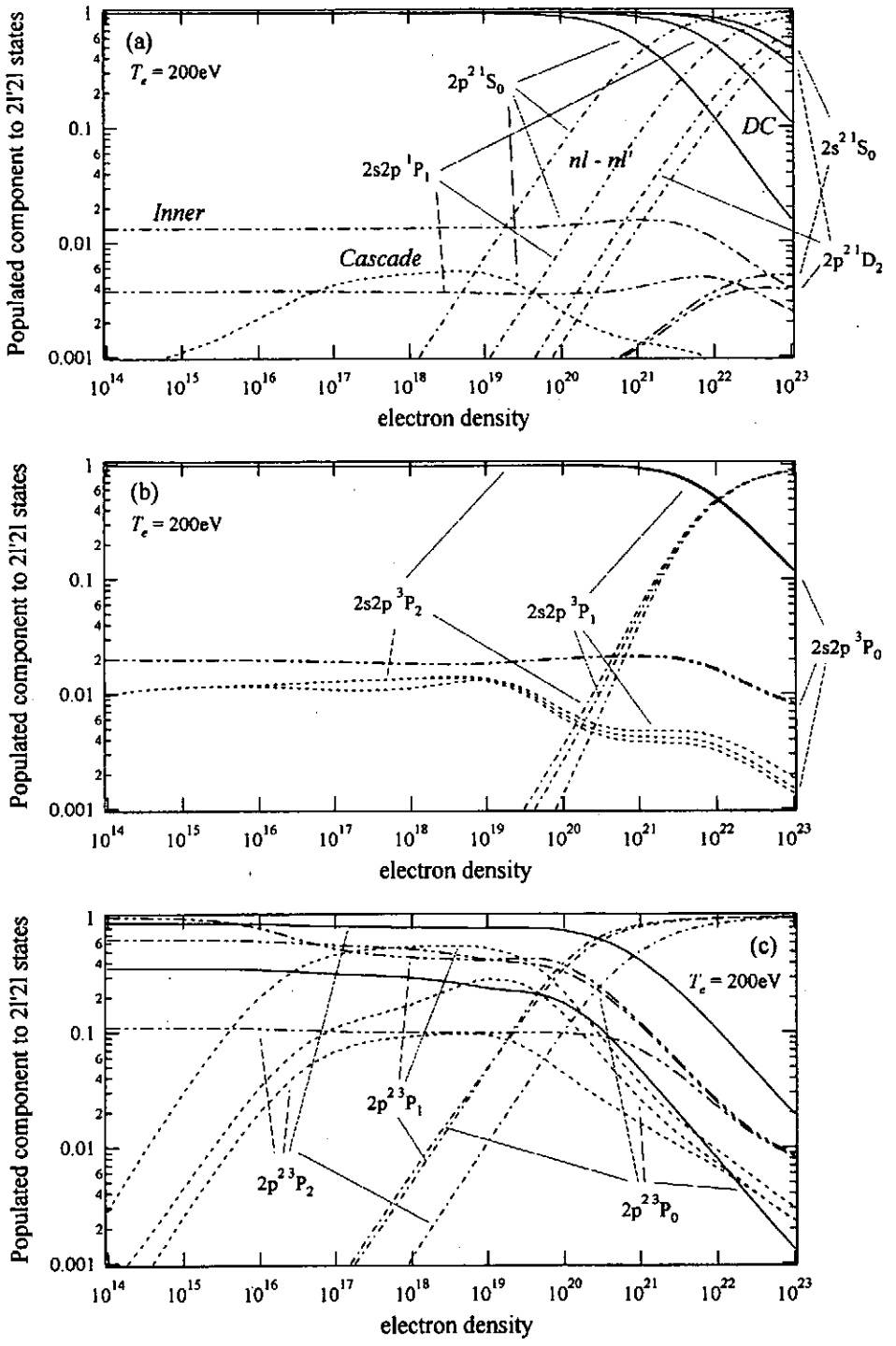

Figure 8. Density dependence of components in population densities of $2l2l'$ states by various processes, dielectronic capture $1s + e^- \rightarrow 2l'nl$ (solid lines), cascade $2l'nl \rightarrow 2l2l'$ and $3lnl' \rightarrow 2l2l'$ (dotted lines), l-changing transition $2l2l' + e^- \rightarrow 2l2l'' + e^-$ (dot-dashed lines), and inner-shell excitations $1s2l + e^- \rightarrow 2l2l' + e^-$ (dot-dot-dashed lines) in ionization equilibrium. (a) $2s^2\,{}^1S_0$, $2s2p\,{}^1P_1$, $2p^2\,{}^1S_0$, and $2p^2\,{}^1D_2$. (b) $2s2p\,{}^3P_{0,1,2}$. (c) $2p^2\,{}^3P_{0,1,2}$.

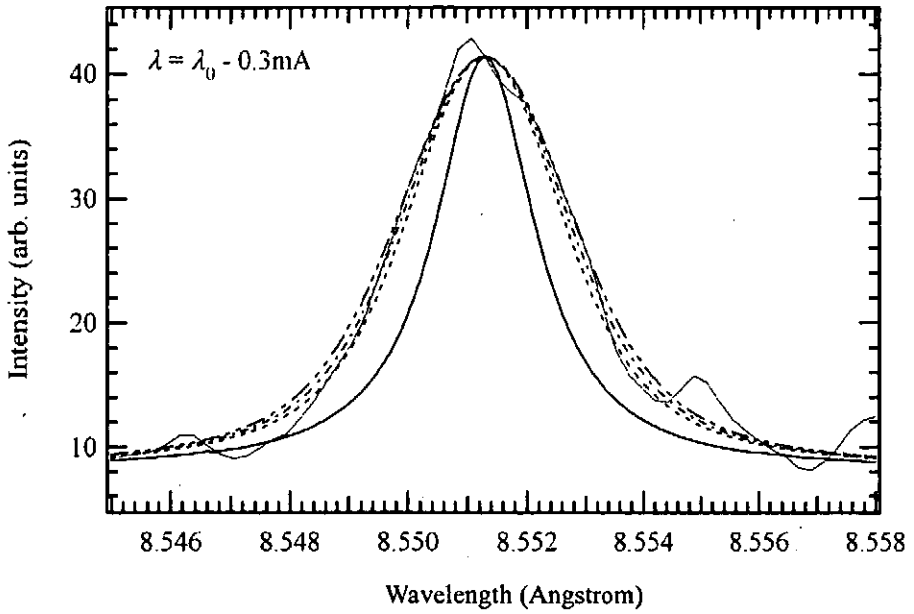

Figure 9. Comparison with the measured spectra (thin line) and theoretical spectra (bold lines) of line J. Line profile for various ion temperatures is shown. The solid line indicates the profile with natural width by spontaneously decay and with instrumental width w = 0.5mÅ only. The dotted, dot-dashed, dot-dot-dashed lines are for ion temperature T_i = 200, 250, 300eV with instrumental width w = 0.5mÅ and natural width. Background intensity is 8.0a.u. Electron temperature and density are assumed to be 200eV and $10^{20}cm^{-3}$, respectively.

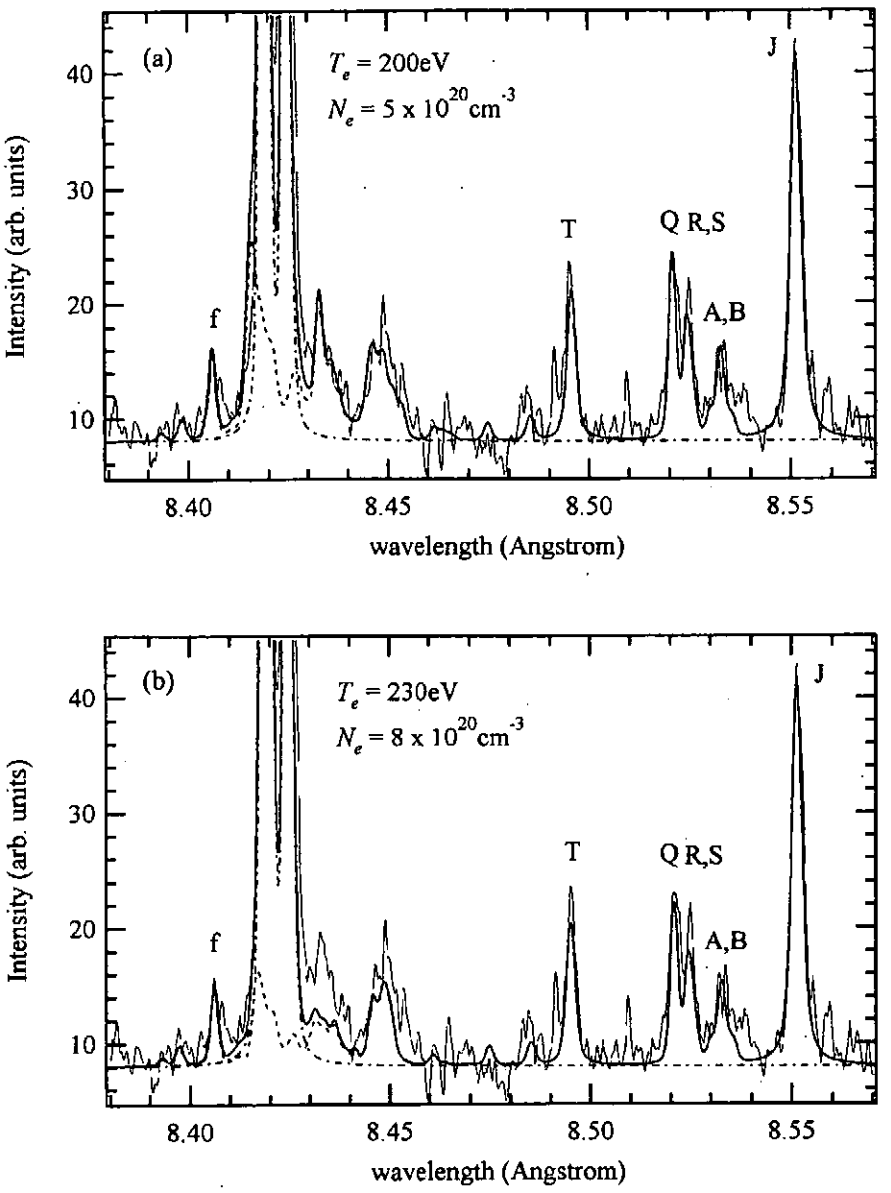

Figure 10. The observed (thin line) and theoretical spectra (bold lines) from "center". Solid, dashed, and dot-dashed lines are the sum of satellite lines and Lyα, the sum of all the satellite lines $1snl - 2l'nl$ (n = 2, 3, 4, and 5), Lyα lines. Instrumental width w is 0.5mÅ. (a) with atomic data by MZ. T_e = 200eV, T_i = 200eV, and $N_e = 5 \times 10^{20}$cm^{-3}. (b) with atomic data by MBL. T_e = 230eV, T_i = 200eV, and $N_e = 8 \times 10^{20}$cm^{-3}.

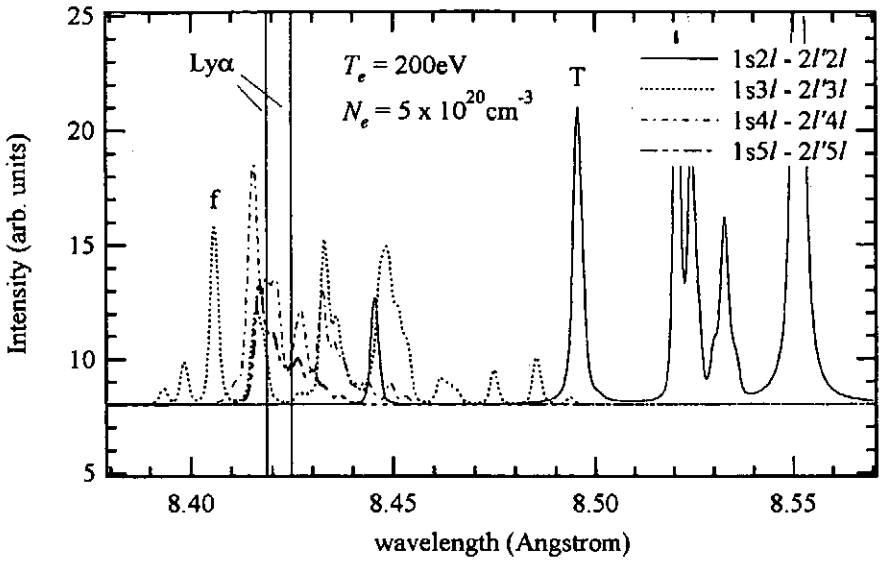

Figure 11. The theoretical line spectra showing the contribution from different components with MZ atomic data. Solid, dotted, dot-dashed, and dot-dot-dashed lines indicate 1s2*l* – 2*l*'2*l*, 1s3*l* – 2*l*'3*l*, 1s4*l* – 2*l*'4*l*, and 1s5*l* – 2*l*'5*l* satellite lines, respectively. T_e = 200eV, T_i = 200eV, $N_e = 5 \times 10^{20}$cm^{-3}, and w = 0.5mÅ.

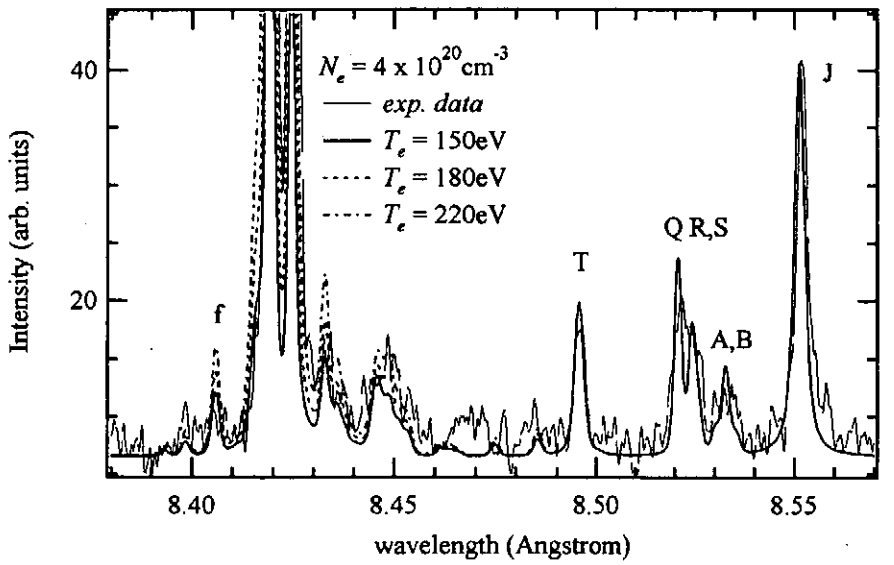

Figure 12. The observed (thin line) and theoretical spectra (thick lines) with atomic data by MZ from "–170μm". Solid, dashed, and dot-dashed lines are the sum of satellite lines and Lyα at T_e = 150eV, 180eV, and 220eV and $N_e = 4 \times 10^{20}$cm^{-3}, respectively. Instrumental width w is 0.5mÅ and T_i = 200eV.

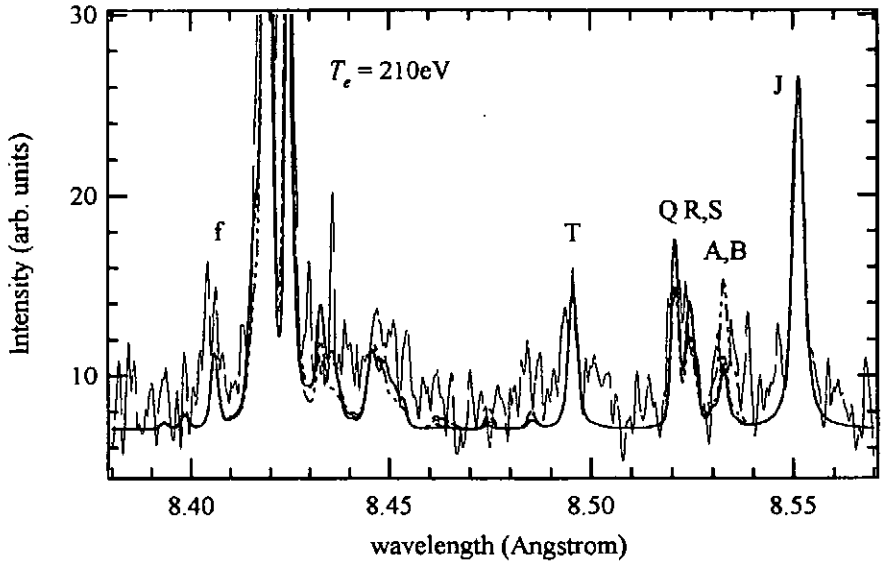

Figure 13. The observed (thin line) spectra from "+170μm" and theoretical (Bold lines) spectra with MZ data for T_e = 210eV. Solid, dotted, dot-dashed, and dot-dot-dashed lines are N_e =10^{19}, 10^{20}, 3×10^{20}, and 3×10^{21}cm^{-3}, respectively.

Symbol	Transition	Wavelength (Å) [4]
$Ly\alpha_1$	$1s\ ^2S_{1/2} - 2p\ ^2P_{3/2}$	8.4246
$Ly\alpha_2$	$1s\ ^2S_{1/2} - 2p\ ^2P_{1/2}$	8.4192
A	$1s2p\ ^3P_2 - 2p^2\ ^3P_2$	8.5327
B	$1s2p\ ^3P_1 - 2p^2\ ^3P_2$	8.5301
Q	$1s2s\ ^3S_1 - 2s2p\ ^3P_2$	8.5208
R	$1s2s\ ^3S_1 - 2s2p\ ^3P_1$	8.5243
S	$1s2s\ ^3S_1 - 2s2p\ ^3P_0$	8.5259
T	$1s2s\ ^1S_0 - 2s2p\ ^1P_1$	8.4956
J	$1s2p\ ^1P_1 - 2p^2\ ^1D_2$	8.5513
f	$1s3d\ ^1D_2 - 2p3d\ ^1F_3$	8.4060

Table 1. The wavelengths and configuration for satellite lines with symbols

Transition		λ (Å)			A^r (s^{-1})			A^a (s^{-1})			Q^d (s^{-1})		
LS-coupling	key	MZ	MBS	MBL	MZ	MBS	MBL	MZ	MBS	MBL	MZ	MBS	MBL
$1s2p\ ^1P_1$-$2p2p\ ^1S_0$		8.4455	8.4450	8.4456	1.90E+13	1.90E+13	2.13E+13	1.78E+13	1.70E+13	1.60E+13	9.19E+12	8.96E+12	9.15E+12
$1s2s\ ^1S_0$-$2s2p\ ^1P_1$	T	8.4956	8.4952	8.4951	1.26E+13	1.25E+13	1.30E+13	2.02E+14	2.04E+14	1.68E+14	3.56E+13	3.53E+13	3.61E+13
$1s2s\ ^3S_1$-$2s2p\ ^3P_2$	Q	8.5208	8.5202	8.5209	1.22E+13	1.21E+13	1.28E+13	1.36E+13	1.15E+13	1.40E+13	3.22E+13	2.95E+13	3.34E+13
$1s2s\ ^3S_1$-$2s2p\ ^3P_1$	R	8.5243	8.5237	8.5244	1.22E+13	1.21E+13	1.28E+13	1.37E+13	1.19E+13	1.51E+13	1.94E+13	1.80E+13	2.08E+13
$1s2s\ ^3S_1$-$2s2p\ ^3P_0$	S	8.5259	8.5252	8.5260	1.22E+13	1.22E+13	1.28E+13	1.36E+13	1.21E+13	1.62E+13	6.44E+12	6.07E+12	7.13E+12
$1s2p\ ^3P_1$-$2p2p\ ^3P_2$	A	8.5301	8.5295	8.5301	6.16E+12	6.08E+12	6.26E+12	2.20E+12	1.53E+12	1.53E+12	2.54E+12	1.80E+12	1.80E+12
$1s2p\ ^3P_2$-$2p2p\ ^3P_2$	B	8.5327	8.5321	8.5327	1.82E+13	1.81E+13	1.86E+13	2.20E+12	1.53E+12	1.53E+12	7.52E+12	5.37E+12	5.35E+12
$1s2p\ ^1P_1$-$2p2p\ ^1D_2$	J	8.5513	8.5497	8.5513	2.44E+13	2.42E+13	2.60E+13	3.71E+14	3.54E+14	3.05E+14	1.15E+14	1.13E+14	1.20E+14
$1s3d\ ^1D_2$-$2p3d\ ^1P_1$		8.3984	8.3967	8.3973	1.08E+13	1.13E+13	1.14E+13	5.09E+12	5.44E+12	2.23E+12	9.68E+12	1.07E+13	5.33E+12
$1s3d\ ^3D_2$-$2p3d\ ^1F_3$	f	8.4053	8.4058	8.4053	1.63E+12	6.28E+11	9.17E+11	2.60E+13	2.49E+13	1.53E+13	7.55E+12	2.88E+12	3.42E+12
$1s3d\ ^1D_2$-$2p3d\ ^1F_3$	f	8.4060	8.4065	8.4060	1.15E+13	1.24E+13	1.24E+13	2.60E+13	2.49E+13	1.53E+13	5.33E+13	5.69E+13	4.63E+13
$1s3p\ ^1P_1$-$2s3d\ ^1D_2$		8.4160	8.4169	8.4167	5.15E+12	5.66E+12	5.44E+12	7.34E+13	7.80E+13	5.09E+13	2.38E+13	2.62E+13	2.41E+13
$1s3s\ ^1S_0$-$2p3s\ ^1P_1$		8.4181	8.4177	8.4180	6.83E+12	6.94E+12	6.69E+12	9.37E+13	9.49E+13	7.23E+13	1.86E+13	1.90E+13	1.78E+13
$1s3p\ ^3P_2$-$2p3p\ ^1D_2$		8.4331	8.4311	8.4364	4.43E+12	1.21E+11	2.78E+12	5.47E+13	4.54E+12	5.35E+13	1.82E+13	3.36E+11	1.16E+13
$1s3p\ ^3P_2$-$2s3d\ ^3D_2$		8.4336	8.4329	8.4318	4.26E+11	6.25E+12	2.01E+11	3.15E+12	2.87E+13	3.39E+12	6.86E+11	2.13E+13	4.91E+11
$1s3p\ ^3P_2$-$2p3p\ ^3P_2$		8.4361	8.4356	8.4336	5.54E+12	3.83E+12	7.02E+12	4.16E+13	5.76E+13	2.54E+13	2.17E+13	1.59E+13	2.30E+13
$1s3p\ ^1P_1$-$2p3p\ ^1D_2$		8.4468	8.4448	8.4501	4.98E+12	1.31E+11	5.41E+12	5.47E+13	4.54E+12	5.35E+13	2.05E+13	3.63E+11	2.25E+13
$1s3p\ ^1P_1$-$2s3d\ ^3D_2$		8.4473	8.4465	8.4455	4.74E+10	2.95E+12	4.73E+10	3.15E+12	2.87E+13	3.39E+12	7.64E+10	1.01E+13	1.16E+11

Table 2. Comparison with atomic data, which are wavelength (λ), radiative transition rate (A^r), autoionization rate (A^a), and intensity factor (Q^d) among three differential codes, which are MZ [11, 16], MBL [18], and MBS [19].

Transition		λ (Å)			A^r (s^{-1})			A^a (s^{-1})			Q_d (s^{-1})		
LS-coupling	key	MZ	MBS	MBL	MZ	MBS	MBL	MZ	MBS	MBL	MZ	MBS	MBL
$1s3d\ ^3D_3$-$2p3d\ ^3F_4$		8.4487	8.4475	8.4482	1.28E+13	1.27E+13	1.31E+13	5.33E+12	5.01E+12	4.39E+12	3.38E+13	3.23E+13	2.96E+13
$1s3p\ ^1P_1$-$2p3p\ ^3P_2$		8.4497	8.4493	8.4473	3.48E+12	4.80E+12	2.25E+12	4.16E+13	5.76E+13	2.54E+13	1.36E+13	1.99E+13	7.38E+12
$1s3d\ ^3D_2$-$2p3d\ ^3F_3$		8.4512	8.4499	8.4507	9.03E+12	9.99E+12	9.98E+12	5.33E+12	5.03E+12	4.41E+12	1.86E+13	1.99E+13	1.76E+13
$1s3d\ ^3D_1$-$2p3d\ ^3F_2$		8.4535	8.4524	8.4532	9.40E+12	8.18E+12	8.81E+12	4.93E+12	4.11E+12	3.74E+12	1.31E+13	1.00E+13	9.81E+12
$1s4d\ ^1D_2$-$2p4d\ ^1F_3$		8.4143	8.4156	8.4163	1.07E+13	1.20E+13	1.18E+13	1.10E+13	1.27E+13	8.09E+12	3.45E+13	4.16E+13	3.16E+13
$1s4f\ ^1F_3$-$2p4f\ ^1D_2$		8.4145	8.4156	8.4163	7.89E+12	1.15E+13	1.23E+13	1.38E+11	4.35E+12	1.28E+12	4.11E+11	1.47E+13	5.53E+12
$1s4f\ ^3F_2$-$2p4f\ ^3D_1$		8.4157	8.4159	8.4168	1.27E+13	1.25E+13	1.28E+13	2.37E+13	2.25E+10	7.35E+09	2.48E+13	6.73E+10	2.20E+10
$1s4f\ ^3F_3$-$2p4f\ ^3D_2$		8.4157	8.4176	8.4182	7.19E+12	6.23E+12	7.96E+12	2.37E+13	8.91E+12	1.66E+12	2.34E+13	1.35E+13	4.60E+12
$1s4f\ ^3F_4$-$2p4f\ ^3D_3$		8.4157	8.4178	8.4186	1.17E+13	8.25E+12	8.20E+12	2.37E+13	2.98E+10	1.15E+10	5.33E+13	1.37E+11	5.20E+10
$1s4f\ ^1F_3$-$2p4f\ ^3D_2$		8.4158	8.4177	8.4183	4.15E+12	3.29E+11	4.30E+08	2.37E+13	8.91E+12	1.66E+12	1.35E+13	7.15E+11	2.49E+08
$1s4p\ ^1P_1$-$2s4d\ ^1D_2$		8.4201	8.4204	8.4212	5.70E+12	4.07E+12	5.90E+12	3.71E+13	2.40E+13	2.36E+13	2.41E+13	1.51E+13	2.23E+13
$1s4s\ ^1S_0$-$2p4s\ ^1P_1$		8.4203	8.4202	8.4208	6.95E+12	6.75E+12	6.34E+12	3.82E+13	3.54E+13	2.65E+13	1.70E+13	1.61E+13	1.41E+13
$1s4p\ ^3P_1$-$2p4p\ ^1D_2$		8.4268	8.4258	8.4299	3.02E+12	8.04E+11	3.34E+11	2.06E+13	2.09E+12	2.33E+13	1.11E+13	6.38E+11	1.28E+12
$1s4d\ ^3D_3$-$2p4d\ ^3F_4$		8.4326	8.4308	8.4316	1.19E+13	9.96E+12	9.91E+12	9.93E+12	1.86E+12	1.58E+12	4.87E+13	1.41E+13	1.23E+13
$1s4p\ ^1P_1$-$2p4p\ ^1D_2$		8.4329	8.4317	8.4358	3.92E+12	5.44E+11	5.47E+12	2.06E+13	2.09E+12	2.33E+13	1.44E+13	4.32E+11	2.09E+13
$1s4p\ ^1P_1$-$2s4d\ ^3D_2$		8.4351	8.4352	8.4313	2.37E+12	5.77E+12	3.83E+09	1.16E+13	2.56E+13	7.26E+11	7.80E+12	2.22E+13	1.47E+09
$1s4d\ ^3D_2$-$2p4d\ ^3F_3$		8.4353	8.4332	8.4340	7.36E+12	7.65E+12	7.40E+12	8.13E+12	2.19E+12	1.87E+12	2.06E+13	8.74E+12	7.30E+12

Transition		λ (Å)			A^r (s^{-1})			A^a (s^{-1})			Q_d (s^{-1})		
LS-coupling	key	MZ	MBS	MBL	MZ	MBS	MBL	MZ	MBS	MBL	MZ	MBS	MBL
$1s5f\ ^3F_3$-$2p5f\ ^3D_2$		8.4168	8.4185	8.4192	7.25E+12	4.25E+09	5.89E+12	1.20E+13	8.98E+11	4.68E+11	1.75E+13	1.40E+09	1.03E+12
$1s5f\ ^3F_2$-$2p5f\ ^3D_1$		8.4168	8.4175	8.4183	1.29E+13	1.26E+13	1.28E+13	1.21E+13	2.42E+09	5.28E+09	1.87E+13	7.25E+09	1.58E+10
$1s5f\ ^3F_4$-$2p5f\ ^3D_3$		8.4168	8.4187	8.4194	1.19E+13	5.86E+12	5.81E+12	1.21E+13	3.82E+09	5.50E+09	4.01E+13	1.24E+10	1.75E+10
$1s5f\ ^1F_3$-$2p5f\ ^3D_2$		8.4169	8.4184	8.4192	4.23E+12	5.93E+11	4.85E+10	1.20E+13	8.98E+11	4.68E+11	1.02E+13	1.96E+12	8.51E+09
$1s5d\ ^1D_2$-$2p5d\ ^1F_3$		8.4170	8.4178	8.4186	8.83E+12	1.13E+13	7.22E+12	5.58E+12	6.58E+12	2.99E+12	2.04E+13	2.67E+13	9.39E+12
$1s5s\ ^1S_0$-$2p5s\ ^1P_1$		8.4209	8.4199	8.4212	7.42E+12	7.06E+12	6.96E+12	1.88E+13	1,68E+13	1.15E+13	1.50E+13	1.36E+13	1.15E+13
$1s5p\ ^1P_1$-$2p5p\ ^1D_2$		8.4211	8.4210	8.4216	7.84E+12	7.03E+12	7.67E+12	2.43E+13	1.97E+13	1.62E+13	2.91E+13	2.44E+13	2.43E+13
$1s5d\ ^3D_3$-$2p5d\ ^3F_4$		8.4260	8.4261	8.4229	1.21E+13	5.28E+12	8.33E+12	4.70E+12	4.41E+11	7.85E+11	3.05E+13	3.61E+12	6.44E+12
$1s5p\ ^1P_1$-$2s5d\ ^1D_2$		8.4275	8.4271	8.4301	3.05E+12	2.70E+11	3.70E+12	7.64E+12	8.32E+11	6.13E+12	9.03E+12	1.63E+11	1.02E+13
$1s5d\ ^3D_2$-$2p5d\ ^3F_3$		8.4292	8.4281	8.4289	5.81E+12	5.49E+12	5.18E+12	3.23E+12	1.12E+12	8.90E+11	8.34E+12	3.78E+12	2.82E+12
$1s5p\ ^1P_1$-$2s5d\ ^3D_2$		8.4298	8.4300	8.4278	1.95E+12	4.09E+12	1.88E+11	4.81E+12	8.53E+12	5.12E+11	6.30E+12	1.25E+13	8.17E+10

Publication List of NIFS Series

NIFS-DATA-71 S. Zou, L. Pichl, M. Kimura and T. Kato
Total, Partial and Differential Ionization Cross Sections in Proton-hydrogen Collisions at Low Energy
Jan. 2003

NIFS-DATA-72 M. Hayashi
Bibliography of Electron and Photon Cross Sections with Atoms and Molecules Published in the 20th Century – Argon –
Jan. 2003

NIFS-DATA-73 J. Horacek, K. Houfek, M. Cizek, I. Murakami and T. Kato
Rate Coefficients for Low-Energy Electron Dissociative Attachment to Molecular Hydrogen
Feb. 2003

NIFS-DATA-74 M. Hayashi
Bibliography of Electron and Photon Cross Sections with Atoms and Molecules Published in the 20th Century
– Carbon Dioxide –
Apr. 2003

NIFS-DATA-75 X. Ma, H.P. Liu, Z.H. Yang, Y.D. Wang, X.M. Chen, Z.Y. Liu, I. Murakami and C. Namba
Cross-section Data Measured at Low Impact Energies for Ar^{q+} Ions on Argon and Neon Targets
Apr. 2003

NIFS-DATA-76 M. Hayashi
Bibliography of Electron and Photon Cross Sections with Atoms and Molecules Published in the 20th Century
– Sulphur Hexafluoride –
May 2003

NIFS-DATA-77 M. Hayashi
Bibliography of Electron and Photon Cross Sections with Atoms and Molecules Published in the 20th Century
– Nitrogen Molecule –
June 2003

NIFS-DATA-78 A. Iwamae, T. Fujimoto, H. Zhang, D. P. Kilcrease, G. Csanak and K.A. Berrington
Population Alignment Collisional Radiative Model for Helium-like Carbon:
Polarization of Emission Lines and Anisotropy of the Electron Velocity Distribution Function in Plasmas
Aug. 2003

NIFS-DATA-79 M. Hayashi
Bibliography of Electron and Photon Cross Sections with Atoms and Molecules Published in the 20th Century – Xenon –
Sep. 2003

NIFS-DATA-80 M. Hayashi
Bibliography of Electron and Photon Cross Sections with Atoms and Molecules Published in the 20th Century – Halogen Molecules –
Dec. 2003

NIFS-DATA-81 M. Hayashi
Bibliography of Electron and Photon Cross Sections with Atoms and Molecules Published in the 20th Century – Water vapour –
Dec. 2003

NIFS-DATA-82 M. Hayashi
Bibliography of Electron and Photon Cross Sections with Atoms and Molecules Published in the 20th Century – Hydrogen molecules –
Feb. 2004

NIFS-DATA-83 M. Hayashi
Bibliography of Electron and Photon Cross Sections with Atoms and Molecules Published in the 20th Century
- Hydrogen Halide Molecules -
Mar. 2004

NIFS-DATA-84 K. Ohya, A. Chen, J. Kawata, K. Nishimura, D. Kato, T. Tanabe and T. Kato
ELECTRAN - Monte Carlo Program of Secondary Electron Emission from Monoatomic Solids under the Impact of 0.1 - 10 keV Electrons
Mar. 2004

NIFS-DATA-85 I. Murakami, T. Kato, U.I. Safronova and A.A. Vasilyev
Dielectronic Recombination Rate Coefficients to Excited States of Boronlike Oxygen and Dielectronic Satellite Lines
May 2004

NIFS-DATA-86 I. Murakami , J. Yan , H. Sato , M. Kimura , R. K. Janev , T. Kato
Collision Processes of Li^{3+} with Atomic Hydrogen: Cross Section Database
Aug. 2004

NIFS-DATA-87 M. Hayashi
Bibliography of Electron and Photon Cross Sections with Atoms and Molecules Published in the 20th Century
- Ammonia and Phosphine -
Aug. 2004

NIFS-DATA-88 N. Yamamoto, T. Kato and F.B. Rosmej
Opacity Free and Space Resolved X-ray Diagnostics Based on Satellinte Lines near H-like Lyα of Highly Charged Ions
Sep. 2004